Proceedings of ASME Turbo Expo 2011
GT2011
June 6-10, 2011, Vancouver, British Columbia, Canada

GT2011-46837

LARGE EDDY SIMULATION OF A HOT, HIGH SPEED COFLOWING JET

Simon Eastwood
Research Associate,
Whittle Laboratory
University of Cambridge
Cambridge, UK, CB3 0DY

Paul G. Tucker
Professor of Engineering
Whittle Laboratory
University of Cambridge
Cambridge, UK, CB3 0DY
Email: pgt23@cam.ac.uk

Hao Xia
Senior Research Fellow
Osney Laboratory
University of Oxford
Oxford, UK, OX2 2ES

ABSTRACT

Computations are made of a short cowl coflowing jet nozzle with a bypass ratio $8:1$. *The core flow is heated, making the inlet conditions reminiscent of those for a real engine. A large eddy resolving approach is used with a* 12×10^6 *cell mesh. Since the code being used tends towards being dissipative the sub-grid scale (SGS) model is abandoned giving what can be termed Numerical Large Eddy Simulation (NLES). To overcome near wall modelling problems a hybrid NLES-RANS (Reynolds Averaged Navier-Stokes) related method is used. For* $y^+ \leq 60$ *a* $k-l$ *model is used. Blending between the two regions makes use of the differential Hamilton-Jabobi (HJ) equation, an extension of the eikonal equation. Results show encouraging agreement with existing measurements of other workers. The eikonal equation is also used for acoustic ray tracing to explore the effect of the mean flow on acoustic ray trajectories, thus yielding a coherent solution strategy.*

1 Introduction

A significant problem of Reynolds Averaged Navier-Stokes (RANS) models for jets is that different constants are required for the near and far fields. No satisfactory solution to this has been found in the last thirty years. More recently, the turbulence modeling community has largely ignored jet modeling problems. [1] outline the difficult task of using RANS to model the substantially different flow physics of isothermal, non-isothermal, sub and super sonic jets for a range of complex nozzle geometries.

In contrast to the problems of RANS, Large Eddy Simulation (LES) can, even on quite coarse grids [2, 3] predict correct trends. As discussed by [4] a compelling case for the use of LES can be made for momentum, heat and mass transfer in free shear flows. In this case, the transport processes of interest are effected by the resolved large scale motions with a cascade of energy from the resolved large scales to the statistically isotropic and universal small scales. In jet shear layers small scales have little influence on the large [5] suggesting the modeling of back scatter, as facilitated by more advanced LES models, is relatively unimportant. In a turbulent jet, most downstream noise is generated by large structures at the tip of the potential core. There are therefore strong reasons to expect LES to be successful in, for example, capturing the major noise sources. Several studies have proven the potential of LES for jets; see for example [3, 6–12]. [13] review the status of jet predictions using LES. The majority of these simulations do not include the nozzle geometry in the domain, an imposed velocity profile preferred instead.

Many industrial Computational Fluid Dynamics (CFD) solvers naturally display dissipative qualities. As discussed by [14] and [15] the low order numerical discretisations frequently used can be as influential as the subgrid scale (SGS) model. This means it can be difficult to disentangle the effect of numerics and SGS modelling. Since the code being used here, as with the majority of industrial based solvers, tends towards being dissipative, omitting the SGS model can be helpful, otherwise excessive dissipation can occur [2]. Model free computations can be termed Implicit LES (ILES) and have been shown to capture well some complex jet dynamics [11]. [2] successfully use ILES

reminiscent simulations for jet predictions. In the current work the SGS model is also omitted. However following [4], the term Numerical LES (NLES) is used rather than ILES. The implication being that the numerical elements of the scheme are active, no claim being made that the numerical contributions represent an especially good SGS model.

More recently, there has been work towards coupling the jet plume to the explicit nozzle geometry. Examples of this include, amongst others, axisymmetric [6, 16–18], coflowing [19–24], bevelled [25,26] and chevron jets [27,28]. Modelling the nozzle boundary layer is challenging, for example there are numerous small near wall streak like structures. These require fine, computationally expensive, cross stream grids. However, the instabilities and turbulence in the shear layer are much stronger than in the boundary layer [22]. Hence, transition is most strongly influenced by the thickness of the boundary layer. A hybrid RANS-LES type approach can accurately capture the bulk properties of the boundary layer, with perhaps the most common realization of this being the Detached Eddy Simulation (DES) method of [29]. In the current work, the $k-l$ model of [30] is used near walls with NLES being used away from walls. The method circumvents near wall streak resolution issues. The disparate length scales in the two zones are blended using a (differential) Hamilton-Jacobi (HJ) equation, an extension to the eikonal equation.

To create a consistent numerical framework, the eikonal equation is also used for acoustic post processing. The eikonal equation is the high frequency limit to the wave equation [31] and can also be used for acoustic ray tracing. The human ear is most sensitive to frequencies in the range 2000 to $4000Hz$, corresponding to acoustic wavelengths $\lambda = 0.1 - 0.2m$. Since the exhaust jet diameter of a real engine is larger, $D \simeq 2-3m$, than λ then the short wave approximation of the eikonal equation is satisfied. Given the flow distribution from a CFD solution, the eikonal equation can directly give acoustic wave fronts and hence the direction of acoustic rays. [32] solve the eikonal equation for propagation of a plane wave through a viscous compressible vortex showing encouraging agreement with benchmark solutions. [31] and [1] directly solve the eikonal equation using the method of [33] to explore the physics of noise release from jets. This jet noise physics exploration process is followed here.

2 Numerical Method

2.1 Governing Equations

The Navier-Stokes equations are solved in their compressible form. Hence conservation of momentum can be expressed using Eq. (1) below:

$$\frac{\partial \rho \tilde{u}_i}{\partial t} + \frac{\partial \rho \tilde{u}_i \tilde{u}_j}{\partial x_j} = -\frac{\partial \tilde{p}}{\partial x_j} + \frac{\partial \tilde{\tau}_{ij}}{\partial x_j} \tag{1}$$

where $\tilde{u}_i$ is fluid velocity, ρ density, μ viscosity (evaluated from Sutherland's equation), $\tilde{p}$ static pressure, t time and x the spatial coordinate. The stress tensor, $\tilde{\tau}_{ij}$ is given by:

$$\tilde{\tau}_{ij} = 2(\mu + \mu_T)\left[\tilde{S}_{ij} - \frac{1}{3}\frac{\partial \tilde{u}_j}{\partial x_j}\delta_{ij}\right] \tag{2}$$

where δ_{ij} is the Kronecker delta. The strain rate tensor is expressed as:

$$\tilde{S}_{ij} = \frac{1}{2}\left(\frac{\partial \tilde{u}_i}{\partial x_j} + \frac{\partial \tilde{u}_j}{\partial x_i}\right) \tag{3}$$

The tilde and T subscript in the above help identify that near walls, traditional RANS averaging is assumed and that elsewhere NLES is implemented. Hence, in the RANS region, $\mu_T = \mu_t$, the eddy viscosity. In the NLES region effectively, μ_T is the numerical diffusion since $\mu_t = 0$. Along with the above, the following energy equation is solved:

$$\frac{\partial \tilde{E}}{\partial t} + \frac{\partial}{\partial x_j}(\tilde{u}_j(\tilde{E} + \tilde{p})) = \frac{\partial}{\partial x_j}(\tilde{u}_i \tilde{\tau}_{ij}) - \frac{\partial \tilde{q}_j}{\partial x_j} \tag{4}$$

with the total energy per unit volume expressed as:

$$\tilde{E} = \rho e + \frac{1}{2}\rho \tilde{u}_i \tilde{u}_i \tag{5}$$

In the above $e = c_v \tilde{T}$ where c_v is the constant volume specific heat capacity. Pressure, temperature and density are related through the equation of state for a perfect gas, $\tilde{p} = \rho R \tilde{T}$. For the heat flux, $\tilde{q}$, the following is used:

$$\tilde{q} = -(k_l + k_T)\frac{\partial \tilde{T}}{\partial x_j} \tag{6}$$

In the above, k_l is the thermal conductivity and $k_T = c_p \mu_T / Pr_T$ where c_p is the specific heat capacity at constant pressure and $Pr_T = 0.9$ is the turbulent Prandtl number. It follows that in the NLES zone, since $\mu_T = 0$, $k_T = 0$. The continuity equation to go with the above is:

$$\frac{\partial \rho}{\partial t} + \frac{\partial \rho \tilde{u}_j}{\partial x_j} = 0. \tag{7}$$

2.2 Solution of the Governing Equations

The unstructured, cell vertex Rolls-Royce plc HYDRA code [34] is used for the calculations. The flux at the control volume interface is based on the flux difference ideas of [35]. The inviscid flux at a control volume face, Φ_f, is expressed as

$$\Phi_f = \frac{1}{2}(\Phi_L + \Phi_R) - \frac{1}{2}|A|[\phi_L - \phi_R] \tag{8}$$

where $A = \partial\Phi/\partial\phi$ (ϕ represents primitive variables) and the subscripts L and R represent variables based on information to the left and right hand side of the face. Here, following [36] Φ_L and Φ_R are simply taken as the adjacent nodal values i.e. $(\Phi_L+\Phi_R)/2$ represents a standard 2^{nd} order central difference. The smoothing term is also approximated in a 2^{nd} order fashion as

$$\frac{1}{2}|A|[\phi_L - \phi_R] = \frac{1}{2}\varepsilon|A|[\tilde{\nabla}^2_L\phi - \tilde{\nabla}^2_R\phi] \tag{9}$$

where $\tilde{\nabla}^2_L$ and $\tilde{\nabla}^2_R$ are undivided Laplacians evaluated at the node locations L and R. The parameter ε is a tunable constant the standard HYDRA value being 0.5. Following [2] the ε term has the static spatially varying distribution shown in figure 1. To help prevent reflection of spurious waves the smoothing is a minimum in the most active turbulent regions and increases towards the domain boundaries. To aid stability smoothing is also increased at the nozzle exit. Too low a value of ε is not helpful for accuracy since dispersion error becomes significant. Based on basic round jet studies, the ε level was reduced to be as low as possible without excessive numerical dispersion error arising. The term $|A|$ in Eq.(8) involves differences (and summations) between the local convection velocity and speed of sound. As the Mach number tends to unity key terms in $|A|$ become small. However, near walls $|A|$ becomes large. This will contaminate LES scales but here, helpfully, they are covered by the RANS layer. For the temporal discretisation, an explicit 5-stage Runge-Kutta scheme is used.

As shown by [37] the numerical viscosity for the current scheme (for homogeneous, decaying turbulence) is of the same order of magnitude as that provided by the Smagorinsky SGS model. This is consistent with the expectations of [15] and [14] who show that for a second order numerical scheme and a standard filter size the numerical contribution will dominate that of the LES model.

2.3 Near Wall Modelling

An LES practice is to take the modelled turbulence length scale as min $(C_s\Delta, \kappa y)$ [38] where C_s and κ are the Smagorinsky and Karman constants respectively. For an LES type grid this will introduce (mixing length) RANS modelling for $y^+ << 60$.

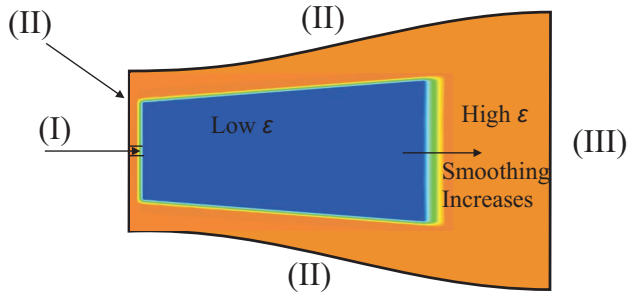

(a) VARIATION OF SMOOTHING FUNCTION AND BOUNDARY CONDITIONS.

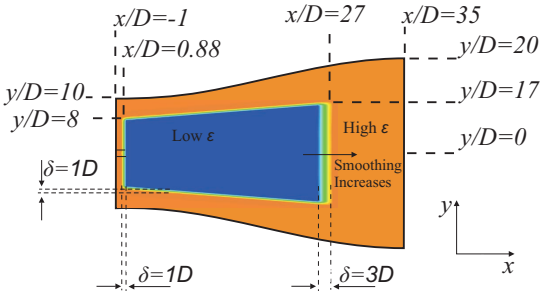

(b) LOCATION OF THE BOUNDARY CONDITIONS.

FIGURE 1. IMPOSED BOUNDARY CONDITIONS AND VARIATION OF SMOOTHING FACTOR ε, WHERE BLUE REGION SHOWS LOWER SMOOTHING AND ORANGE THE HIGHEST SMOOTHING.

Here, to reduce grid demands but still maintain the higher LES fidelity we switch between RANS and NLES at $y^+ \approx 60$, covering over just the near wall streak structures having the finest scales. Hence the switch is much closer to the wall than for DES (where the whole boundary layer is RANS modelled) but further out than for LES. This, it is believed, gives a good compromise between accuracy and computational efficiency for jets. Validation of the current approach can be found in [39].

For the near wall RANS region, the $k-l$ model of [30] is used for which we have extensive in depth methods validation for boundary layers and a range of other flow types. Following [22], and to save computational time, the developed/converged RANS layer is frozen. The modelled turbulent kinetic energy, k, equation is as follows:

$$\frac{\partial \rho k_T}{\partial t} + \frac{\partial \rho u_i k_T}{\partial x_i} = \frac{\partial}{\partial x_j}\left[\left(\mu + \frac{\mu_T}{\sigma_k}\right)\frac{\partial k_T}{\partial x_j}\right] + P_{k_T} - \frac{\rho {k_T}^{3/2}}{l_\varepsilon} \tag{10}$$

where P_{k_T} is the turbulence production term. In the NLES region

$k_T = k_{sgs} = 0$. For the RANS region:

$$\mu_T = \rho C_\mu l_\mu {k_T}^{1/2} \tag{11}$$

where the length scale of equation (11) is given by:

$$l_\mu = C_l \tilde{d}(1 - e^{-A_\mu y^*}) \tag{12}$$

and the length scale of equation (10) is given by:

$$l_\varepsilon = C_l \tilde{d}(1 - e^{-A_e y^*}) \tag{13}$$

In the above $\tilde{d}$ is normal wall distance or modified function of it (see later). Constants have following standard values; $C_l = 2.4, A_\mu = 0.016, A_e = 0.263$ and $\sigma_k = 1.0$ (the diffusion Prandtl number for k).

2.4 Eikonal Equation

The eikonal equation is given by equation 14;

$$c^2 |\nabla \varphi| = 1 \tag{14}$$

where c is a front speed and the dependent variable φ models propagating acoustic front arrival times. For $c = 1$, the first front arrival times are equal to wall distance, d, the variable needed in the turbulence model. If c is sound speed, acoustic ray fronts are gained in a stationary medium. The eikonal equation is solved in the integrated HYDRA framework as detailed and extensively validated ([32]). First, use of the eikonal equation for turbulence modelling is considered.

2.4.1 Turbulence Modelling

For the near wall RANS region, d is required, whereas in the NLES region d is zero. To facilitate this, the separate variable, $\tilde{d}$ is defined, where in the RANS region, $\tilde{d} = d$ and in the NLES region $\tilde{d} = 0$. The equation (14) variable φ is now made equivalent to the modified wall distance, $\tilde{d}$, and wave fronts have unit velocity. The distance function $\tilde{d}$ is evaluated from the Hamilton Jacobi (HJ) equation:

$$|\nabla \tilde{d}| = 1 + f(\tilde{d}) \nabla^2 \tilde{d} + g(d) \tag{15}$$

The first two terms of Eq. 15 give the eikonal equation, which gives the d needed for the RANS zone. The blending between the RANS and LES zones is achieved by the addition of a Laplacian (given by the third term). In Eq. (15) these are the following functions: $f(\tilde{d}) = \varepsilon_0 \tilde{d}$ and $g(d) = \varepsilon_1 (d/L)^n$. The length scale L is the distance from the wall to the NLES region, and n is a positive integer. The function $f(\tilde{d})$ forces the Laplacian to tend to zero near walls. The function $g(d)$ helps to bias the blending. Figure 2(a) shows various distributions which can be formed for different ε_0 and ε_1. The HJ equation can be solved for directly in HYDRA and is used here with $n \simeq 4$, $\varepsilon_0 \simeq 1.2$ and $\varepsilon_1 \simeq 7.5$. The RANS layer is also algebraically cropped at the nozzle exit plane so that it does not extend into the shear layer. [12] explored the influence of different values for n, ε_0 and ε_1. Results were found to be relatively insensitive to the precise smoothing parameters used. Hence here, a smoothing profile which lies in the middle of the range explored in [12] is used.

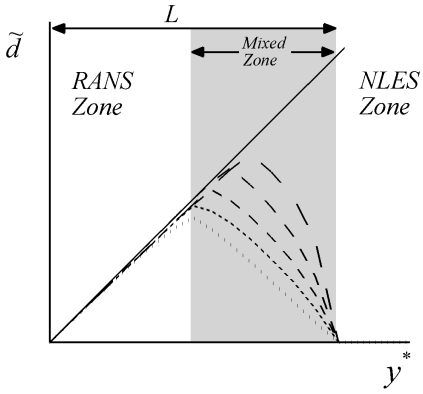

(a) POTENTIAL BLENDING PROFILES.

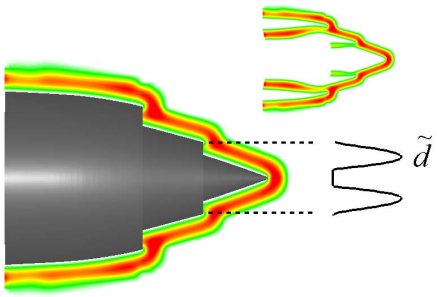

(b) $\tilde{d}$ CONTOURS.

FIGURE 2. WALL DISTANCE PLOTS SHOWING (a) POTENTIAL BLENDING PROFILES OF REQUIRED WALL DISTANCE BETWEEN RANS AND NLES REGIONS. AND (b) CONTOURS OF $\tilde{d}$. INSET SHOWS CONTOURS INSIDE THE NOZZLE.

2.4.2 Acoustic Ray Tracing

For acoustic ray tracing a source term, given by the third term in equation (16) below, is added to the eikonal equation where u gives the velocity field from a preceding CFD calculation.

$$c^2 |\nabla \varphi| = 1 - (u \nabla \varphi) \tag{16}$$

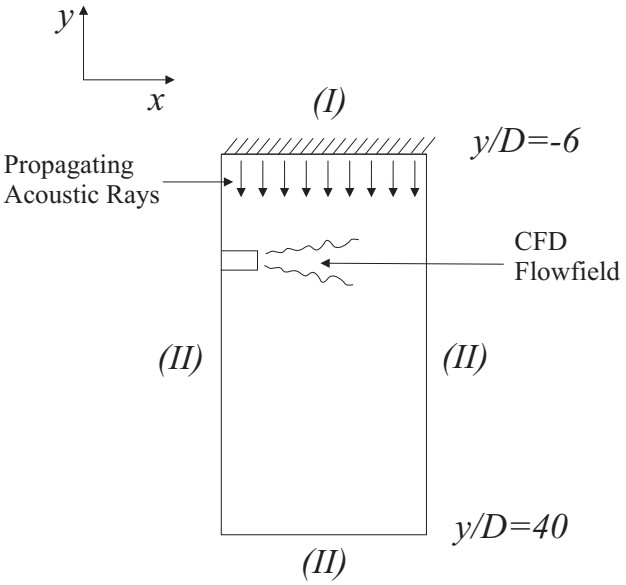

(a)

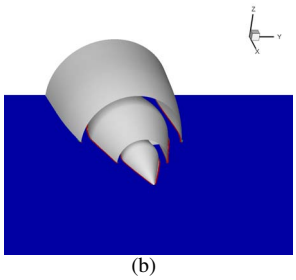

(b)

FIGURE 3. SCHEMATIC SHOWING PROPAGATION OF ACOUSTIC RAYS TOWARDS THE JET FLOW.

To avoid Godunov front flattening [40] (where the grid structure strongly reduces curvature in certain zones) the flow solution is interpolated onto an rectangular domain populated with an unstructured tetrahedral cells (this randomises the flattening allowing for potential cancellation errors). The mesh is scaled to give a jet nozzle diameter similar to that of a real engine. Figure 3 shows a schematic of the arrangement. For boundaries labelled (II) φ is extrapolated from interior values and for boundary (I) $\varphi = 0$ corresponding to a planar wave source.

3 Case Set-Up

3.1 Geometry and Mesh

Figure 4 gives a schemetic of the nozzle geometry. Figure 5 shows the mesh in the $x-y$ plane and also in the $y-z$ plane at $x/D = 1$. Meshes which maintain orthogonality between the control volume face and the line which connects the nodes that straddle that face tend to give better energy conservation properties. The first off wall grid node is set at an average of $y^+ = 1.0$. This is more than adequate for the $k-l$ model with its algebraically prescribed length scale and a first off wall grid location of $4 \times 10^{-5} D$. The nozzle has a blunt nose. Here an H-Block is embedded to avoid an axis singularity on the jet centreline.

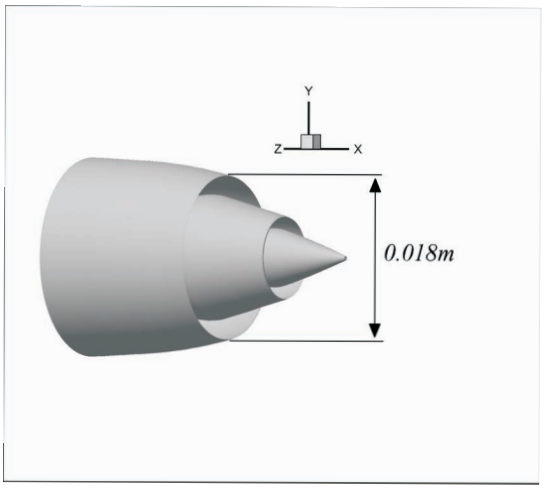

FIGURE 4. SHORT COWL CO-FLOWING NOZZLE.

For the current 12×10^6 cell mesh, there are 60 nodes radially in both the core and bypass flows. Axially, from the bypass inlet to the nozzle tip there are 100 nodes. From the nozzle tip to $x/D = 4$ are a further 150 nodes. There are 150 azimuthal nodes giving a total, in this region, of 4.5×10^6 cells. This gives Δx^+ and Δr^+ values of 300 and 150 in the nozzle at the bypass and core exits. A further 4.5×10^6 are used from $x/D = 4$ to 8. The remaining nodes are used further downstream and radially outside the nozzle. At $x/D = 1$ (the nozzle tip is at $x/D = 0.88$), there are about 30 nodes across the outer shear layer and roughly 35 nodes across the inner shear layer. At $x/D = 3$ the shear layers have merged to form one shear layer. Here, there are in the region of about 40 grid points across the shear layer. It should be stressed that for an isothermal equivalent of the current case a grid independence study was performed on a 50×10^6 cell case (see [39]). This work confirms the adequacy of the current grid i.e. there is a 15% variation in the typical profiles shown later in this work.

3.2 Boundary Conditions

The operating conditions are summarised in table 1. The Reynolds number is 300,000 (based on the nozzle diameter, D, and maximum jet velocity in the bypass flow, U_s). The exit Mach numbers are matched to those of a real jet engine with the exit velocity of the core and bypass $480 ms^{-1}$ and $306 ms^{-1}$ respectively. The static temperature in the core and bypass flows is $775K$ and $288K$ respectively. The boundary conditions are labeled in figure 1. Both core and bypass inlets (boundary (I)) are prescribed

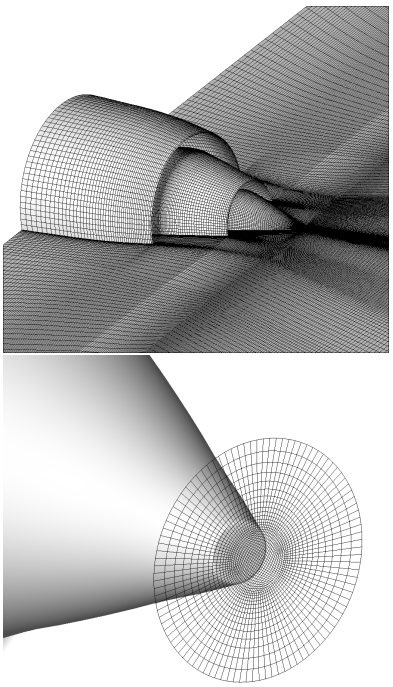

FIGURE 5. MESH IMAGES AROUND THE NOZZLE AND IN THE $X-Y$ PLANE IN THE TOP FRAME AND IN THE $Y-Z$ PLANE IN THE BOTTOM FRAME.

as subsonic inlets. Avoiding spurious waves in mind, no forcing is applied. The Kelvin-Helmholtz shear layer instabilities develop naturally but can be slightly delayed relative to when we use synthetic turbulence [39]. This also prevents the introduction of arbitrary parameters. No velocity profiles are specified at the nozzle inlet. The boundary layers develop naturally to give boundary layer thicknesses of around 0.02 D (see [18]) for both the core and bypass nozzle exits.

At boundary (III), a subsonic outlet is prescribed. This boundary is located 35 D downstream of the jet exit. At boundary (II), a freestream condition is used. Near to the boundaries the smoothing is increased to help prevent reflection of spurious waves. Figure 1(b) shows the domain boundaries and where the smoothing increases. The parameter δ gives the distance over which the smoothing increases. Also, the nozzle walls are viscous.

3.3 Solution Time

The simulation is run from quiescent initialisation. The physical timestep of the simulation is approximately 0.2×10^{-8} s based on the smallest cell size. This gives a maximum CFL number of approximately 0.5 in the near nozzle region. Based on the bypass jet diameter and peak velocity, this gives t^* $(=ut/D)$ of approximately 3×10^{-5}. Hence a single t^* requires $35,000$ physical timesteps. There are potential time savings from using an implicit solver but this was not made use of here. The solution runs on a Cray $XT4$. The system uses AMD 2.3 GHz Opteron processors giving a theoretical peak performance of 208 Tflops. Using 128 cores, approximately $75,000$ timesteps can be completed in 12 hours. A mature solution is gained over 100 t^* and averaged over a further 100 t^*. Hence the complete simulation takes approximately 2 months on 128 cores.

TABLE 1. JET FLOW CONDITIONS

	Conditions	
U_p	$480ms^{-1}$	Velocity of Primary Flow
U_s	$306ms^{-1}$	Velocity of Bypass Flow
M_p	0.861	Mach Number of Primary Flow
M_s	0.902	Mach Number of Bypass Flow
T_p	$775K$	Static Temperature in Primary Flow
T_s	$288K$	Static Temperature in Bypass Flow

4 Validation

Isothermal predictions for the current nozzle are reported in [18]. Here, since there is extension to hot jets some further validation is considered appropriate. Hence some single stream validation cases are considered. Effectively, the short cowl and inner spinner of the figure 4 nozzle as well as the nozzle curvature are removed. A two block axisymmetric grid topology is used. An inner H-Block with $302\times26\times26$ nodes is used to prevent an axis singularity from occurring at the jet axis. An outer O-Block is used with $342\times104\times98$ nodes in the streamwise, radial and azimuthal directions. The grid is $45D$ long in x and extends $15.5D$ radially from the jet centreline at $x/D=-5$. The domain flares outwards with axial extent so that at $x/D=40$ the mesh extends $24D$ radially. The nozzle exit is $5D$ downstream of the domain boundary at $x/D=0$. Broadly the same boundary conditions are used as for the dual stream case.

Solutions are run for $t^*=200$ to gain a mature flow solution. Time averaging is completed over a further $500t^*$. The jets develop from approximate top hat velocity profiles. To calculate fourth order correlation coefficients on the jet shear layer, time histories of variables are recorded on the jet shear layer every timestep. Spatially, information is recorded at discrete points from $x/D=1$ to 11 with equal spacing, Δx, of $0.05D$. Information is recorded on 4 shear layers spaced equally in the azimuthal direction. Hence values are circumferentially averaged over the 4 planes. Correlations about the points $x/D=2,4,6,8$ and 10 are calculated. The fourth order correlation coefficient is given by:

TABLE 2. HOT JETS STUDIED.

Identifier	Ma_j	Ma_∞	U_j	T_j/T_∞
$C1$	0.9	0.826	282	0.83
$H1$	0.6	0.816	270	1.6
$H2$	0.88	1.11	380	1.5
$H3$	0.81	1.375	470	2.3

$$R_{ij,kl} = \overline{r'_{i(x+\Delta x,t+\Delta t)} r'_{j(x+\Delta x,t+\Delta t)} r'_{k(x,t)} r'_{l(x,t)}} \quad (17)$$

where $'$ indicates a fluctuating quantity, x is the streamwise location, t is time, r is a correlated variable (which here is a velocity component multiplied by density, ρ) and R is the correlation coefficient. i,j,k,l can be $1,2$ or 3, giving 3 components of velocity. Hence $R_{11,11}$ gives $R_{uu,uu}$, the fourth order correlation of the streamwise velocity. The 4^{th} order correlation is a key parameter in characterising the noise sources.

Total pressure and temperature are modified at the jet inlet to explore the conditions shown in Table 2. Ma_j is the jet Mach number, Ma_∞ is the acoustic Mach number (the ratio of the jet exit velocity to the ambient speed of sound), U_j is the jet exit velocity and T_j/T_∞ the ratio of the jet exit temperature to the ambient temperature. The jet diameter is modified to maintain $\mathrm{Re} = 10,000$ for all cases.

Figure 6 plots, for case $C1$, fourth order correlations of streamwise velocity fluctuations. The correlations are taken about the point $x/D = 4.0$. Lines plot the predictions and symbols the measurements of Harper-Bourne [41]. The encouraging agreement gives some confidence that the simulation has captured the flow physics of the jet turbulence which describes the acoustic sources. The Reynolds number and Mach number of the Harper-Bourne data (2×10^5 and 0.18) is **different** from the current simulation (1×10^4 and 0.9), hence the results suggest that the correlation shapes are not sensitive to the jet parameters. Other correlations about $x/D = 2,6,8$ and 10 show similar agreement.

Figure 7a plots centreline velocity decay of the time averaged streamwise velocity for cases $C1$ and $H1-H3$. Lines show predictions and symbols measurements of [42]. The changes in trends for the predictions and measurements are the same with both showing the potential core length to decrease with heating. Figure 7b plots centreline momentum decay for all the cases with lines again showing predictions. Here there are no measurements available. The graph shows the momentum decay to be the same for all cases, indicating that the change in potential core length in figure 7a is due to density effects. For hot jets, as fluid exits the nozzle into the cold ambient it begins to cool, resulting in an increase in density and a corresponding decrease in velocity.

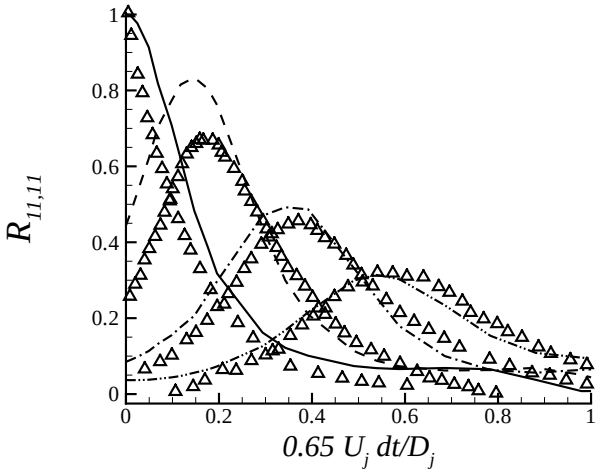

FIGURE 6. FOURTH ORDER CORRELATION COEFFICIENTS AT $x/D = 4$ for Case $C1$. (—— $\Delta x/D = 0.0$, $- - - -$ $\Delta x/D = 0.2$, $-\cdot-\cdot-$ =$\Delta x/D = 0.4$, $-\cdot\cdot-\cdot\cdot-$ =$\Delta x/D = 0.6$. Δ MEASUREMENTS OF [41].)

This decrease in velocity is coupled with the velocity decay due to mixing, which is the only effect in the cold jet. Hence for hot jets the overall decay is faster. When density and velocity are taken into account, potential core lengths are similar for all cases.

Figure 7c plots centreline normal stress. Measurements, shown by symbols, are available for cases $C1$ and $H3$ only, hence the predictions, shown by lines, are only plotted for these cases. The change in trend of the computations between these two cases is the same as the change in the measurements. With heating, the peak turbulence level is further upstream, corresponding to the shorter potential core length. For the hot jet case, the peak turbulence levels are 10% higher.

Figure 7d plots the peak shear layer shear stress. Linestyles are as in figure 7c. Here, changes in turbulence with heating are less clear. The red dashed lines indicate the uncertainty in the measurements for the cold jet case, $C1$. The change in turbulence with heating, for both measurements and predictions, are within this uncertainty. Generally, the predictions give encouraging agreement for $x/D > 3$.

Far field OASPL (overall sound pressure level) the current predictions are also in encouraging agreement with the measurements of [43]. These results are presented in Appendix. Hence, broadly, it can be seen that the predictive procedure extends adequately to hot jets.

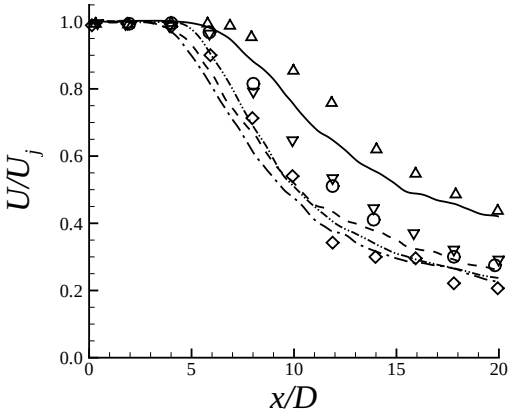

(a) CENTRELINE VELOCITY.

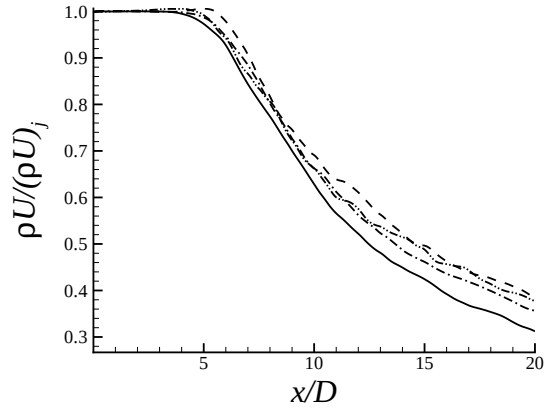

(b) CENTRELINE MOMENTUM.

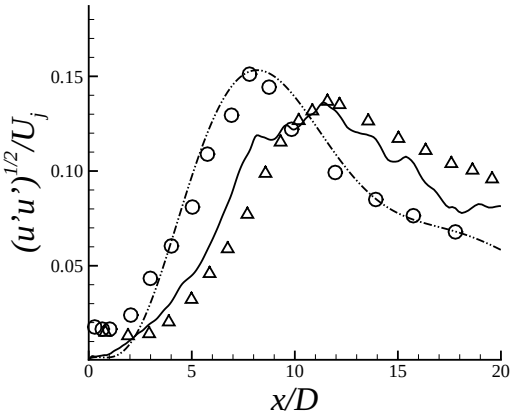

(c) CENTRELINE NORMAL STRESS.

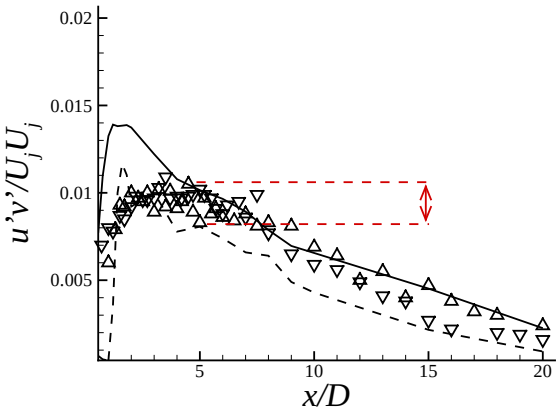

(d) PEAK SHEAR STRESS.

FIGURE 7. AXIAL VARAIATIONS FOR HOT JET CASES OF (a) CENTERLINE VELOCITY, (b) CENTRELINE MOMENTUM, (c) CENTRELINE NORMAL STRESS AND (d) PEAK SHEAR LAYER SHEAR STRESS. LINES ARE PREDICTIONS RESULTS WHERE —— $C1$, – – – – $H1$, – · – · – $H2$, – · · – · · – $H3$. SYMBOLS ARE MEASUREMENTS OF [42] WHERE Δ $C1$, ∇ $H1$, $\diamond$ $H2$, $\circ$ $H3$.

5 Co-flow Nozzle Results

Figure 8(a) shows vorticity isosurfaces. These give a qualitative impression of the flow. The coherent structures associated with the initial shear layer roll up can just be observed. This can then be seen to rapidly breakdown into turbulence with substantial anisotropy and fine scales. Substantial anisotropy can be seen. The isosurfaces are coloured by density, showing the darker, lower density region in the hot jet core. Figure 8(b) shows time averaged streamwise velocity. The two shear layers produced by the coflowing jet can be seen.

Figure 9 plots radial profiles of mean streamwise velocity, normal and shear stresses, temperature and momentum at axial locations $x/D = 1.43$, 2.52, 3.25, 4.70, 6.16 and 7.25. Full lines show the NLES-RANS results and symbols measurements of [24]. For the axial velocity, shown in frame (a), there is encouraging agreement between the computations and measurements. At $x/D = 3.98$ two sets of measurements are plotted, taken in the $x-y$ and $x-z$ planes. As can be seen the measurement inconsistency suggests a probable lack of symmetry [44] discuss flow asymmetry effects in coflowing jets noting that, especially for heated jets, axisymmetry is virtually impossible to achieve. As can be seen from the figure, the current asymmetry results in a probable measurement uncertainty of at least 8%. For $x/D > 4.0$ the computations under-predict the measurements on the centreline but are within the uncertainty of the measurements. At $x/D = 1.43$ both measurements and computations show a velocity deficit on the centreline, which is also visible

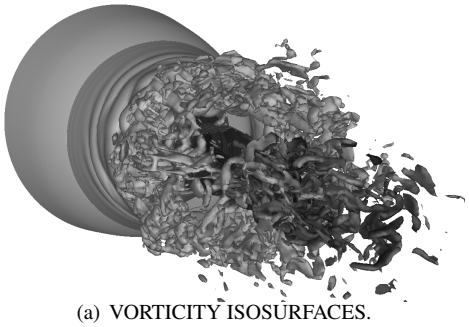

(a) VORTICITY ISOSURFACES.

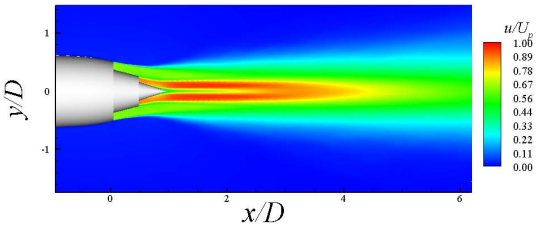

(b) STREAMWISE VELOCITY

FIGURE 8. FLOW VISUALISATION IMAGES OF (a) VORTICITY ISOSURFACES AND (b) TIME AVERAGED COUTOUR PLOTS OF STREAMWISE VELOCITY

in the figure 8(b) contour plot of mean streamwise velocity. Previous work by the current authors [45] demonstrated the RANS layer to be helpful in capturing this flow feature through preventing premature separation.

Frame (b) plots normal stress profiles. Again, at $x/D = 3.98$ profiles in two planes are plotted for the measurements. Now, due to the asymmetry, the uncertainty in the measurements is greater, at least 20%. The computations give encouraging results for $x/D > 4.0$ being within the lower limit of uncertainty of the measurements. Computations and measurements show two areas of peak stress, associated with the two shear layers. The outer, at $x/D \simeq 1.5$ and the inner, at $x/D \simeq 2$ 3. The computations substantially overpredict the peak normal stress on both shear layers.

Frame (c) plots shear stress profiles. Measurements are available in one plane. The computations show encouraging agreement, particularly for $x/D > 2.0$. The biggest discrepancy is also on the outer shear layer where again the magnitude is overpredicted. The accuracy of the current results are at least as good as, if not better than, those of other workers.

Frame (d) plots radial profiles of temperature. No measurements are available in this region, the computations being plotted for completeness. There is no temperature gradient between the bypass flow and the ambient, hence the temperature drops to ambient levels by $|y/D| = 0.25$.

Frame (e) plots radial profiles of axial momentum, again no measurements are available. Whilst velocity is higher in the core flow than the bypass the axial momentum peaks in the bypass flow, not the core flow. This is due to the density differences. Hence, by far the biggest propulsive thrust component will be due to the co-flow.

Figure 10 shows contour plots in the $x-y$ plane of normal, shear and radial Reynolds stresses. The normal and shear stresses identify the two shear layers, with the second becoming more intense furthest downstream. Figure 11 plots density gradient magnitude contours. These show vortex roll up on the outer shear layer. The inner shear layer appears more stable and becomes turbulent further downstream. This is consistent with the LES of [19].

Figure 12 plots contours of pressure time derivative for $|y/D| > 1$. For $|y/D| < 1.0$ contours of instantaneous streamwise velocity are overlaid. Acoustic waves emanating from the non-linear flow field can be seen at approximately 30^0 to the mean flow direction.

Use was made of the eikonal equation in the hybrid NLES-RANS approach. To illustrate further the jet acoustics and also the current integrated solution framework it is utilised again to explore the trajectory of high frequency acoustic rays. The rays are propagated in an adjoint sense i.e. the sound sources are seeded outside the jet and their deflection as they pass through the jet is observed. The human ear is sensitive to frequencies in the range of $2,000$ to $4,000Hz$. This corresponds to wavelengths in the range of 0.08 to $0.16m$. For gas turbine aero engines the exhaust jet diameter, D, has a scale of $2-3m$. Hence at full scale the acoustic wavelength will be smaller than key flow scales making the eikonal equation solutions meaningful.

The solid lines in figure 13 represent acoustic rays passing through the time averaged flow field, computed from the eikonal equation. This the high frequency limit of the full acoustic wave propagation equation. Acoustic rays are shown propagating from the centre of the jet at axial locations $x/D = 4$, 8 & 12. At each axial location 10 rays are plotted from $z/D = -1$ to 1 The background contour plot shows the mean streamwise velocity. As can be seen the acoustic rays are strongly deflected (in the streamwise direction) by the flow. The greatest deflection is on the centreline of the jet. The effect of the jet spreading on the acoustic rays can be clearly seen- with increasing x, more rays deviate. This substantial deviation would need to be accounted for in some way when using an acoustic mirror to measure sound sources.

By varying c in the flow field, figure 14 explores the effect of temperature on the acoustic rays. In an adjoint sense the rays are released from the far field and their subsequent deflection as they pass through the jet explored. Solid lines plot rays with c calculated from the CFD solution and dashed with $c = 330m/s$ (i.e. consistent with isothermal flow). The background contour plot shows c calculated from the CFD solution, with c increasing in the core flow. Rays propagate all the way through the jet. For conditions representing heated flow the rays are deflected least.

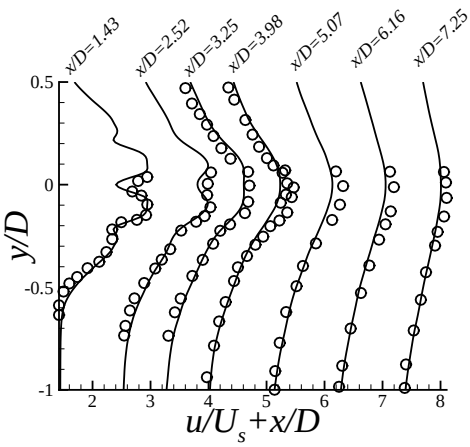

(a) MEAN AXIAL VELOCITY.

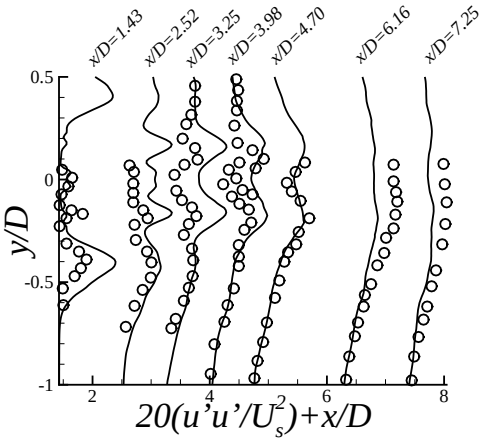

(b) NORMAL STRESS.

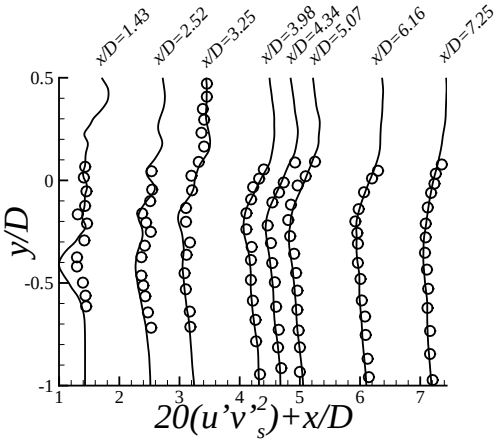

(c) SHEAR STRESS.

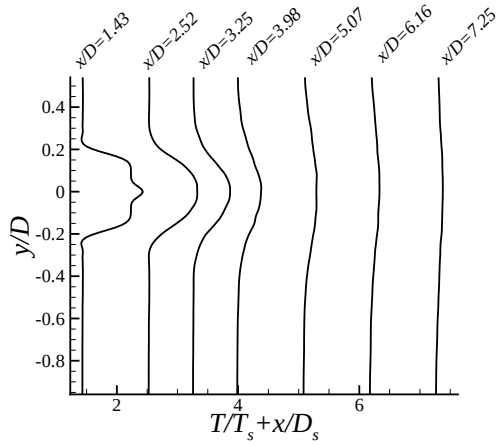

(d) TEMPERATURE.

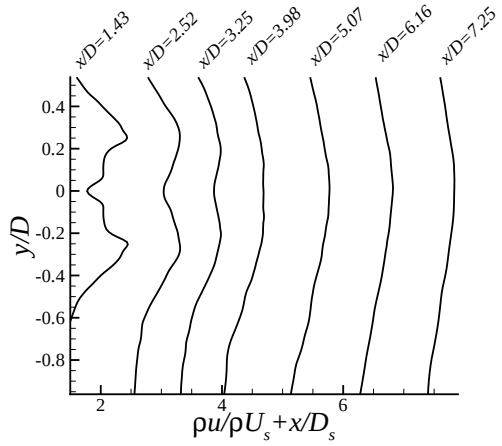

(e) MOMENTUM.

FIGURE 9. RADIAL PROFILES OF: (a) MEAN AXIAL VELOCITY (b) NORMAL STRESS (c) SHEAR STRESS (d) TEMPERATURE AND (e) MOMENTUM AT AXIAL LOCATIONS $x/D = 1.43$ to 7.25. —— NLES-RANS, ○ MEASUREMENTS [24].

This is because the rays pass more quickly through the flow (due to increasing c in the core flow) and are less exposed to the mean flow effects than when c is constant.

6 Conclusion

After initial single stream validation studies, computations were made for a subsonic short cowl coflowing jet nozzle. The core flow was hot with the bypass flow at the same temperature as the surrounding ambient fluid. The computational strategy implemented a $k-l$ RANS model for $y^+ < 60$. An LES related method was used away from the wall. Since the numerical strategy used tended towards being dissipative the subgrid scale

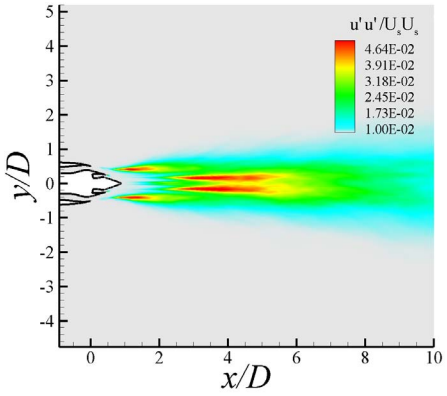

(a) NORMAL STRESS.

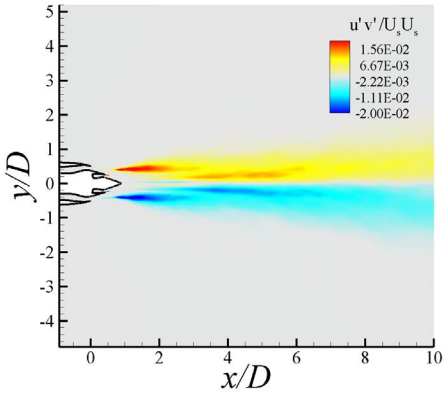

(b) SHEAR STRESS.

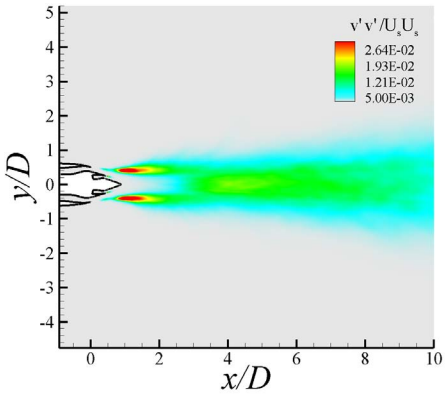

(c) RADIAL STRESS.

FIGURE 10. COUTOUR PLOTS IN THE $x-y$ PLANE OF: (a) NORMAL STRESS, (b) SHEAR STRESS AND (c) RADIAL STRESS

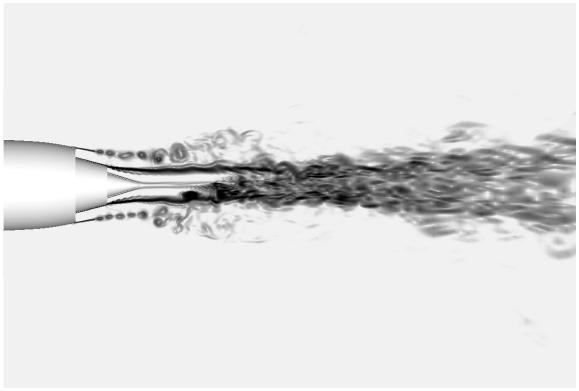

FIGURE 11. DENSITY GRADIENT MAGNITUDE IN $x-y$ PLANE.

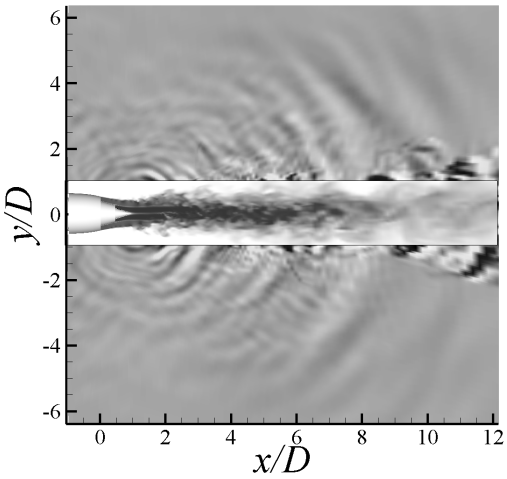

FIGURE 12. CONTOURS OF dp/dt for $|y/D| > 1$ WITH INSTANTANEOUS STREAMWISE VELOCITY OVERLAID FOR $|y/D| < 1$.

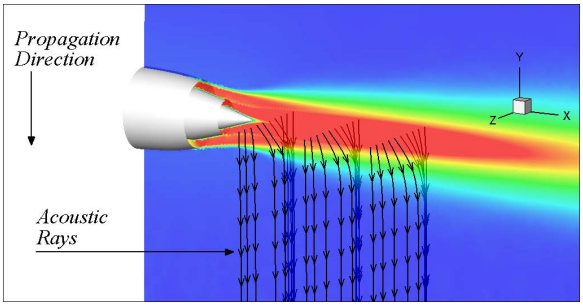

FIGURE 13. A $3-D$ VIEW OF ACOUSTIC RAYS PASSING THROUGH THE JET. ACOUSTIC RAYS ARE PLOTTED AT $x/D =$ 4, 8 &12 AND 10 RADIAL LOCATIONS $z/D = -1.0$ to 1.0.

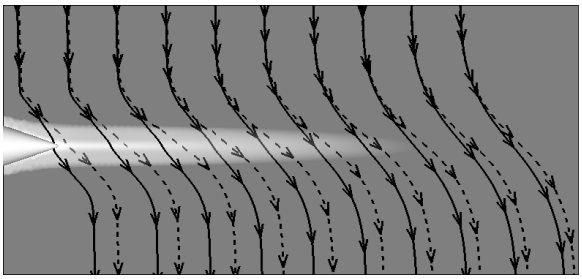

FIGURE 14. ACOUSTIC RAYS PASSING THROUGH THE JET IN THE $x-y$ PLANE. ACOUSTIC RAYS ARE PLOTTED FOR $x/D =$ 0.5 to 5.0

model was abandoned giving what can be termed hybrid NLES-RANS. Blending between the NLES and RANS regions made use of the eikonal equation which was also used to calculate wave fronts, and hence acoustic ray traces, creating an integrated solution approach. The computations showed encouraging agreement with the measurements, demonstrating the usefulness of the hybrid NLES-RANS approach. In terms of streamwise average velocity and turbulence statistics computations were generally within the lower limit of experimental uncertainty. For the Reynold's stresses, the largest discrepancy was in the shear layers where the peak stresses were substantially overpredicted. Again, indicating the usefulness of the hybrid NLES-RANS layer in preventing non-physical separation from the nozzle the velocity deficit on the jet centreline was correctly predicted. Heating is shown to substantially affect the path of high frequency acoustic rays through the jet (deviation of 10%). With heating the acoustic wave speed through the jet is higher and hence rays seem less susceptible to the mean flow effects.

7 Acknowledgments

Funding from the Engineering and Physical Sciences Research Council (EPSRC) is gratefully acknowledged under grant number $GR/T06629/01$. Tucker gratefully acknowledges his Royal Society Fellowship funding and the support of Rolls-Royce plc. High performance computing time was under EPSRC grants EP/F005954/1 & EP/G027633/1.

Appendix

Figure 15 plots OASPL at $100D$ where symbols show the measurements of [43] and lines predictions. Looking at the curves for cases $C1$ and $H1$, the change in trends for the measurements are the same as for the predictions. The agreement of the predictions against measurements is worse for case $H3$ where the peak value is in error by 8dB although for θ from 50° to 90° agreement is within 2dB. Modifying the closing disk used can yield results with a peak value within 1dB of the measurements.

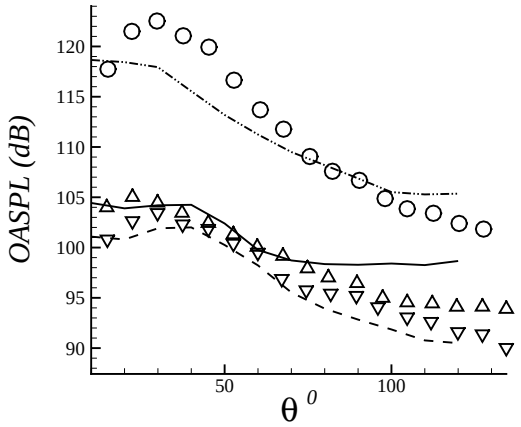

FIGURE 15. OASPL for hot jet cases. Lines are HYDRA results and symbols measurements of [43]

Nomenclature

A_e, A_μ, c_l, c_μ	Turbulence model constants
c	Sound speed
D	Maximum nozzle diameter
$d, \tilde{d}$	Wall distance and modified wall distance
E	Total energy per unit volume
e	Internal energy per unit mass
k, k_T	Turbulent kinetic energy and modelled turbulent kinetic energy
l_ε, l_μ	Modelled turbulence length scales
Ma	Mach number
Ma_j	Jet Mach number
Ma_∞	Acoustic Mach number
Pr	Prandtl Number
Pr_T	Turbulent Prandtl number
P_{kT}	Turbulence production term
p	Pressure
R	Gas constant
Re	Reynolds number based on jet diameter
S_{ij}	Strain rate tensor
T	Temperature
T_p T_s	Primary flow exit temperature and bypass flow exit temperature
t	Solution timestep
t^*	Non dimensional time
U_j	Peak jet exit velocity
U_p, U_s	Primary flow exit velocity and bypass flow exit velocity

Greek Symbols

δ	Kronecker delta
ε	Constant for smoothing

ε_0, ε_1	Tunable constants in Hamilton-Jacobi equation
μ, μ_t, μ_T	Viscosity, eddy viscosity and modelled viscosity
ρ	Density
σ_k	Diffusion Prandtl number for k
τ_{ij}	Stress tensor
Φ, ϕ	Flux and primative variable or nodal values
φ	Propagating front arrival time

Subscripts

f	Control volume face
j	Jet exit
L, R	Left and right hand nodal values
T	Distinguishing different values in RANS and NLES regions
sgs	Subgrid scale
num	Numerical
∞	Ambient
0	Reference

Superscripts

$\bar{}$	Average
$'$	Fluctuating value
$\tilde{}$	Distinguishing different values in RANS and NLES regions

REFERENCES

[1] Secundov, A., Birch, S., and Tucker, P., 2007. "Propulsive jets and their Acoustics.". *Philosophical Transactions of the Royal Society of London. Series A, Mathematical and Physical Sciences.,* **365**, pp. 2443–2468.

[2] Shur, M., Spalart, P., Strelets, M., and Travin, A., 2003. "Towards the prediction of noise from jet engines.". *International Journal of Heat and Fluid Flow,* **24**, pp. 551–561.

[3] Shur, M., Spalart, P., and Strelets, M., 2005. "Noise prediction for increasingly complex jets. part 1: Methods and tests.". *International Journal of Aeroacoustics,* **4**, pp. 213–246.

[4] Pope, S., 2000. *Turbulent Flows.* Cambridge University Press.

[5] Suzuki, T., and Colonius, T., 2006. "Instability Waves in a Subsonic Round Jet Detected Using a Near-Field Phased Microphone Array.". *Journal of Fluid Mechanics,* **000**, pp. 1–30.

[6] Andersson, N., Eriksson, L., and Davidson, L., 2005. "Effects of Inflow Conditions and Subgrid Model on LES for Turbulent Jets.". In 11th AIAA Aeroacoustics Conference, 23-26 May, Monterey, California, 2006. AIAA 2005-2925.

[7] Boersma, B., and Lele, S., 1999. "Large Eddy Simulation of a Mach 0.9 Turbulent Jet.". In 5th AIAA Aeroacoustics Conference, 10-12 May 1999, Bellvue, WA. AIAA 1999-1874.

[8] Bodony, D., and Lele, S., 2004. "Jet Noise Prediction of Cold and Hot Subsonic Jets Using Large Eddy Simulation.". In 10th AIAA Aeroacoustics Conference, 10-12 May 2004, Manchester, United Kingdom. AIAA 2004-3022.

[9] Bogey, C., Bailly, C., and Juve, D., 2003. "Noise Investigation of a High Subsonic, Moderate Reynolds Number Jet Using a Compressible Large Eddy Simulation.". *Theoretical Computational Fluid Dynamics,* **16**, pp. 273–297.

[10] Eastwood, S. J., Tucker, P. G., Xia, H., and Klostermeier, C., 2009. "Developing Large Eddy Simulation for Turbomachinery Applications.". *Philosophical Transactions of the Royal Society of London. Series A, Mathematical and Physical Sciences.,* **367**, pp. 2999–3013.

[11] Grinstein, F., 2006. "Recent Progress on Montone Integrated Large Eddy Simulation of Free Jets.". *JSME International Journal,* **49(4)**, pp. 890–898.

[12] Tucker, P. G., 2004. "Novel MILES Computations for Jet Flows and Noise.". *International Journal of Heat and Fluid Flow,* **25**, pp. 625–635.

[13] Bodony, D., and Lele, S., 2008. "Current Status of Jet Noise Predictions Using Large Eddy Simulation.". *American Institute of Astronautics and Aeronautics,* **46**, pp. 364–380.

[14] Kravchenko, A., and Moin, P., 1997. "On the Effect of Numerical Errors in Large Eddy Simulation of Turbulent Flows.". *Journal of Computational Physics,* **131**, pp. 310–322.

[15] Ghosal, S., 1996. "An Analysis of Numerical Errors in Large Eddy Simulations of Turbulence.". *Journal of Computational Physics,* **125**, pp. 187–206.

[16] Uzun, A., and Hussaini, Y., 2006. "High Frequency Noise Generation in the Near Nozzle Region of a Jet.". In 12th AIAA Aeroacoustics Conference, 8-10 May 2006, Cambridge, Massachusetts, AIAA 2006-2499.

[17] Bogey, C., Barre, S., and Bailly, C., 2008. "Direct Computation of the Noise Generated by Subsonic Jets Originating from a Straight Pipe Nozzle.". *International Journal of Aeroacoustics,* **7**, pp. 1–22.

[18] Eastwood, S. J., Tucker, P. G., Xia, H., Carpenter, P., and Dunkley, P., 2010. "Large Eddy Simulations and Measurements of a Small Scale High Speed Coflowing Jet.". *American Institute of Aeronautics and Astronautics,* **48(5)**, pp. 963–974.

[19] Andersson, N., Eriksson, L., and Davidson, L., 2005. "LES Prediction of Flow and Acoustic Field of a Coaxial Jet.". In 11th AIAA Aeroacoustics Conference, 23-25 May 2005, Monterey, California, AIAA 2005-2884.

[20] Bogey, C., Barre, S., and Bailly, C., 2007. "Direct Computation of the Noise Generated by a Hot Coaxial Jet.". In

13th AIAA Aeroacoustics Conference, 21-23 May, Rome Italy, AIAA 2007-3587.

[21] Mihaescu, M., Szasz, R., and Fuchs, L., 2005. "Numerical Investigation of the Acoustics of a Coaxial Nozzle.". In 43rd AIAA Aerospace Sciences Meeting and Exhibit, 10-13 January, Reno, Nevada. AIAA 2005-420.

[22] Shur, M., Spalart, P., Strelets, M., and Garbaruk, A., 2006. "Further steps in les based noise prediction for complex jets.". In 44th AIAA Aerospace Sciences and Meeting Exhibit, 9-12 January, Reno, Nevada, 2006. AIAA 2006-485.

[23] Vuillot, F., Lupoglazoff, N., and Rahier, G., 2008. "Double Stream Nozzle Flows and Noise Computations and Comparisons to Experiments.". In 46th AIAA Aerospace Sciences Meeting and Exhibit, Reno, Nevada, Jan. 7-10, AIAA-2008-9.

[24] Yan, J., Tawackolian, K., Michel, U., and Thiele, F., 2007. "Computation of Jet Noise using a Hybrid Approach.". In 13th AIAA Aeroacoustics Conference, 21-23 May, Rome Italy, AIAA 2007-3621.

[25] Viswanathan, K., Shur, M., Spalart, P., and Strelets, M., 2008. "Flow and Noise Predictions for Single and Dual Stream Beveled Nozzles.". *American Institute of Aeronautics and Astronautics,* **46(3)**, pp. 601–626.

[26] Paliath, U., and Morris, P., 2005. "Prediction of Noise from Circular Beveled Nozzles.". In 11th AIAA Aeroacoustics Conference, 23-25 May 2005, Monterey, California, AIAA 2005-3096.

[27] Uzun, A., and Hussaini, A., 2007. "Noise Generation in the Near Nozzle Region of a Chevron Nozzle Jet Flow.". In 13th AIAA Aeroacoustics Conference, 21-23 May, Rome Italy, AIAA 2007-3596.

[28] Xia, H., Tucker, P. G., and Eastwood, S. J., 2009. "Large Eddy Simulations of Chevron Jet Flows with Noise Predictions.". *International Journal of Heat and Fluid Flow.* In press.

[29] Spalart, P., 2000. "Strategies for Turbulence Modelling and Simulations.". *International Journal of Heat and Fluid Flow.,* **21**, pp. 252–263.

[30] Wolfshtien, M., 1969. "The Velocity and Temperature Distribution on One Dimensional Flow with Turbulence Augmentation and Pressure Gradient.". *International Journal of Heat and Mass Transfer,* **12**, pp. 301–318.

[31] Khiritov, K., Kozlov, V., Krasheninnikov, S., Lebedev, A., Lyubimov, D., Maslov, V., Mironov, A., Reent, K., Secundov, A., Yakubovsky, K., and Birch, S., 2005. "On the Prediction of Turbulent Jet Noise Using Traditional Aeroacoustic Methods.". *International Journal of Aeroacoustics,* **4**, pp. 289–323.

[32] Tucker, P. G., and Karabasov, S., 2009. "Unstructured Grid Solution Approach for Eikonal Equation with Acoustics in Mind.". *International Journal of Aeroacoustics,* **8(6)**, pp. 535–554. In press.

[33] Landau, L., and Lifshitz, E., 1987. *Fluid Mechanics*. Pergammon.

[34] Lapworth, B., 2004. "HYDRA CFD: A Framework for Collaborative CFD Development.". In International Conference on Scientific and Engineering Computation, Singapore, July 2004.

[35] Roe, P., 1997. "Approximate Riemann Solvers, Parameter Vectors and Difference Solvers.". *Journal of Computational Physics,* **135**, pp. 250–258.

[36] Morgan, K., Peraire, J., and Hassan, O., 1991. "The Computation of Three Dimensional Flows Using Unstructured Grids.". *Computer Methods in Applied Mechanics and Engineering,* **87**, pp. 335–352.

[37] Ciardi, M., Sagaut, P., Klein, M., and Dawes, W., 2005. "A dynamic finite volume scheme for large eddy simulation on unstructured grids.". *Journal of Computational Physics,* **210(2)**, pp. 632–655.

[38] Yang, K., and Ferziger, J., 1993. "Large Eddy Simulation of Turbulent Obstacle Flow Using a Dynamics Subgrid Scale Model.". *American Institute of Aeronautics and Astronautics,* **31(8)**, pp. 1406–1413.

[39] Eastwood, S., 2010. "Hybrid LES-RANS of Complex Geometry Jets". PhD thesis, University of Cambridge.

[40] Tsai, Y., 2002. "Rapid and Accurate Computation of the Distance Function using Grids.". *Journal of Computational Physics,* **178**, pp. 175–195.

[41] Harper-Bourne, M., 2003. "Jet Noise Turbulence Measurements". In 9th AIAA Aeroacoustics Conference, 12-14 May, South Carolina, AIAA 2003-3214.

[42] Bridges, J., and Wernet, M., 2004. Measurements of the aeroacoustic sound sources in hot jets. Tech. rep., NASA Glenn Research Centre, NASA/TM-2004-221508.

[43] Tanna, H., 1977. "An experimental study of jet noise part 1: Turbulent mixing noise.". *Journal of Sound and Vibration,* **50(3)**, pp. 405–428.

[44] Birch, S., Khritov, K., Maslov, V., Mironov, A., and Secundov, A., 2005. "An Experimental Study of Flow Asymmetry in Co-axial Jets.". In 11th AIAA Aeroacoustics Conference, 23-26 May, Monterey, California, 2005. AIAA 2005-2845.

[45] Eastwood, S. J., Tucker, P. G., Xia, H., Carpenter, P., and Dunkley, P., 2008. "Comparison of LES to LDA and PIV Measurements of a Small Scale High Speed Coflowing Jet.". In 14th AIAA/CEAS Aeroacoustics Conference, Vancouver, British Columbia, May 5-7, 2008. AIAA-2008-2981.